OPEN ACCESS



A Hot Jupiter with a Retrograde Orbit Around A Sun-like Star and a Toy Model of Hot Jupiters in Wide Binary Star Systems

Steven Giacalone^{1,16}, Andrew W. Howard¹, Ryan A. Rubenzahl², Fei Dai³, Luke B. Handley¹, Howard Isaacson⁴, Samuel Halverson⁵, Max Brodheim⁶, Matt Brown⁶, Theron W. Carmichael^{3,17}, William Deich⁷, Benjamin J. Fulton⁸, Steven R. Gibson⁹, Grant M. Hill⁶, Bradford Holden⁷, Aaron Householder^{10,11}, Russ R. Laher⁸, Kyle Lanclos⁶, Kyle Lanclos⁶, Joel Payne ⁶, Erik A. Petigura ¹², Arpita Roy ¹³, Christian Schwab ¹⁴, Martin M. Sirk ¹⁵, and Josh Walawender ⁶, Department of Astronomy, California Institute of Technology, Pasadena, CA 91125, USA; giacalone@astro.caltech.edu ² Center for Computational Astrophysics, Flatiron Institute, 162 Fifth Avenue, New York, NY 10010, USA Institute for Astronomy, University of Hawai'i, 2680 Woodlawn Drive, Honolulu, HI 96822, USA ⁴ Department of Astronomy, 501 Campbell Hall, University of California, Berkeley, CA 94720, USA ⁵ Jet Propulsion Laboratory, California Institute of Technology, 4800 Oak Grove Drive, Pasadena, CA 91109, USA W. M. Keck Observatory, 65-1120 Mamalahoa Hwy, Kamuela, HI 96743, USA UC Observatories, University of California, Santa Cruz, CA 95064, USA NASA Exoplanet Science Institute/Caltech-IPAC, California Institute of Technology, Pasadena, CA 91125, USA Caltech Optical Observatories, California Institute of Technology, Pasadena, CA 91125, USA Department of Earth, Atmospheric and Planetary Sciences, Massachusetts Institute of Technology, Cambridge, MA 02139, USA Kavli Institute for Astrophysics and Space Research, Massachusetts Institute of Technology, Cambridge, MA 02139, USA

12 Department of Physics & Astronomy, University of California Los Angeles, Los Angeles, CA 90095, USA Astrophysics & Space Institute, Schmidt Sciences, New York, NY 10011, USA ¹⁴ School of Mathematical and Physical Sciences, Macquarie University, Balaclava Road, North Ryde, NSW 2109, Australia Space Sciences Laboratory, University of California, Berkeley, CA 94720, USA Received 2025 May 30; revised 2025 July 2; accepted 2025 July 7; published 2025 July 28

Abstract

We report an observation of a transit of the hot Jupiter (HJ) KELT-23A b with the Keck Planet Finder spectrograph and a measurement of the sky-projected obliquity (λ) of its Sun-like ($T_{\rm eff}\approx 5900~{\rm K}$) host star. We measured a projected stellar obliquity of $\lambda\approx 180^\circ$, indicating that the orbit of the HJ is retrograde relative to the direction of the stellar spin. Due to the slow sky-projected rotational velocity of the host star ($v\sin i_\star\approx 0.5~{\rm km~s^{-1}}$), the true orbit of the HJ could be closer to polar. HJs around stars with effective temperatures below the Kraft break—such as KELT-23A—are generally found to have prograde orbits that are well-aligned with the equatorial planes of their host stars (i.e., $\lambda\sim 0^\circ$), most likely due to spin-orbit realignment driven by stellar tidal dissipation. This system is therefore a unique outlier that strains migration and tidal theories. The fact that the HJ has a highly misaligned orbit may suggest that the planet arrived at its close-in orbit relatively recently, possibly via interactions with the wide-separation (570 au) M-dwarf companion in the system, or that it has stalled near an antialigned or polar orientation while realigning. Using Gaia DR3, we determined the orbit of the stellar companion to be moderately face-on ($\gamma=60^\circ\pm4^\circ$). We show that the distribution of observed systems in the $\gamma-\lambda$ plane can be broadly reproduced using a toy model in which the orbits of the planetary and stellar companions begin aligned with the equatorial plane of the primary star and, upon migrating inwards, the planet preferentially obtains either an aligned or polar orbit.

Supplementary material for this article is available online

Unified Astronomy Thesaurus concepts: Exoplanet dynamics (490); Exoplanet migration (2205); Star-planet interactions (2177)

Original content from this work may be used under the terms of the Creative Commons Attribution 4.0 licence. Any further distribution of this work must maintain attribution to the author(s) and the title of the work, journal citation and DOI.

1. Introduction

Hot Jupiters (HJs; Jupiter-like planets orbiting close to their host stars) are generally believed to form far from their stars and move inwards via one of two mechanisms: migration through the protoplanetary disk or high-eccentricity tidal migration, the process by which the orbit of the planet is excited into a highly eccentric orbit that subsequently shrinks and circularizes due to tidal interaction with the star near

¹⁶ NSF Astronomy and Astrophysics Postdoctoral Fellow.

¹⁷ NSF Ascend Fellow.

periastron (see Dawson & Johnson 2018 for a review). While the existence of these close-in giants has been known for decades, the dominant mechanism responsible for their observed orbits has long remained a mystery.

Stellar obliquity—the angle between the stellar spin axis and the orbital axis of its transiting planetary companion—contains unique clues about the orbital evolutions of planets. In general, disk migration should primarily result in planet orbits that are roughly coplanar with the equators of their host stars (hereafter referred to as "aligned" orbits) whereas high-eccentricity tidal migration should often result in planets orbits that are significantly inclined relative to the equators of their host stars (hereafter referred to as "misaligned" orbits). An informative summary of the stellar obliquity distributions resulting from different eccentricity-excitation mechanisms can be found in Albrecht et al. (2022).

The sky-projected component of the stellar obliquity (λ) , accessible via the Rossiter-McLaughlin effect (McLaughlin 1924; Rossiter 1924), has become a particularly valuable tool for understanding the origins of HJs (e.g., Rice et al. 2022a; Dong & Foreman-Mackey 2023; Siegel et al. 2023). Winn et al. (2010) identified the first trends in the λ distribution for stars with HJs, finding that these stars tend to have low λ (i.e., aligned orbits) when $T_{\rm eff}$ < 6250 K and often have high λ (i.e., misaligned orbits) when $T_{\rm eff} > 6250$ K. This dichotomy has primarily been interpreted as the consequence of more efficient tidal dissipation around stars cooler than the Kraft break, where stars have radiative interiors and convective exteriors (Albrecht et al. 2012). Because HJs around hotter stars tend to have misaligned orbits, many have argued that high-eccentricity migration offers the most compelling explanation for their close-in orbits.

In this connection, HJs in binary star systems are notable case studies of inward migration. Wide-separation stellar companions are believed to be capable of driving a number of mechanisms that result in misaligned orbits (e.g., Anderson et al. 2016; Yang et al. 2025), including some in which the protoplanetary disk itself is forced into a highly inclined orientation (e.g., Batygin 2012). Given the higher probability of hotter stars belonging to multi-star systems (Moe & Di Stefano 2017), these mechanisms may be partially responsible for the observed λ distribution if they are highly efficient. Over the years, the number of stars with both transiting planets and wide binary stars with measured λ has steadily grown, allowing for the first investigations of the relationship between the orbits of the planetary and stellar companions (Behmard et al. 2022; Rice et al. 2024).

In this paper, we expand this sample with an obliquity measurement of the star KELT-23A, a Sun-like star ($T_{\rm eff} = 5899 \pm 49 \, \text{K}$, $R_{\star} = 0.996 \pm 0.015 \, R_{\odot}$, $M_{\star} = 0.944^{+0.060}_{-0.054} \, M_{\odot}$) with a wide-separation binary M dwarf companion and a transiting HJ on a 2.26 days orbit (Johns et al. 2019). The

paper is organized as follows. In Section 2, we describe the observations used in our analysis of the KELT-23 system. In Section 3, we detail our analysis of the data. In Section 4, we place the KELT-23 system into context by comparing it to other systems. In addition, we present a toy model that can broadly reproduce the observed orientations of systems with both HJs and wide-separation stellar companions. We provide concluding remarks in Section 5.

2. Observations

2.1. Keck Planet Finder Spectroscopy

We observed a transit of KELT-23A b on 2024 April 24 UT using the high-resolution ($R \sim 97,000$) Keck Planet Finder (KPF) spectrograph on the 10 m Keck-I telescope to derive precise radial velocities of the host star (Gibson et al. 2024). Our observations were scheduled via the KPF Community Cadence project (Lubin et al. 2025). We acquired 32 480 s exposures between 9:40 and 14:23 UT with the standard 47 s detector readout, achieving peak signal-to-noise ratios per pixel of 180 in the green arm (445-600 nm) and 220 in the red arm (600-870 nm) after stacking the three science traces. These observations covered the full transit of the HJ, which took place between 10:40 and 13:00 UT, and approximately 1.5 hr of out-of-transit baseline. At the beginning and end of the sequence, we acquired a single wavelength calibration exposure using a Fabry-Pérot etalon in order to track and correct for intranight instrumental drift (Schwab et al. 2015). The data were reduced and radial velocities were derived using the publicly available KPF pipeline. 18 The KPF radial velocities (RVs) are shown in Table 1.

2.2. TESS Photometry

We also utilized time-series photometry of the KELT-23 system from the Transiting Exoplanet Survey Satellite (TESS; Ricker et al. 2015) in the joint fit. TESS observed the system for a total of 19 sectors, each of which spans roughly 27 days in length. Data from each sector was collected as a 2 minutes cadence and was analyzed by the TESS Science Processing Operations Center (Jenkins et al. 2016). Data from seven of the sectors were also collected at a 20 s cadence. The full TESS data set begins in July of 2019 and ends in October of 2024, spanning more than five years.

3. Analysis

3.1. Stellar Obliquity

To measure the projected stellar obliquity (λ) of the system, we jointly fit the TESS photometry and KPF radial velocity data using DYNESTY, a dynamic nested sampler implemented in Python (Speagle 2020). The TESS data were modeled using

¹⁸ https://github.com/Keck-DataReductionPipelines/KPF-Pipeline

Table 1
KPF Radial Velocity Data

Time	RV	$\sigma_{ m RV}$	
(BJD)	$(m s^{-1})$	$(m s^{-1})$	
2460424.90737	-16953.06	1.15	
2460424.91354	-16955.25	1.16	
2460424.91962	-16957.36	1.17	
2460424.92580	-16959.35	1.17	
2460424.93182	-16961.95	1.16	
2460424.93804	-16965.27	1.17	
2460424.94416	-16968.31	1.14	
2460424.95008	-16971.74	1.16	
2460424.95635	-16977.42	1.19	
2460424.96264	-16981.47	1.18	
2460424.96864	-16982.71	1.22	
2460424.97468	-16988.47	1.22	
2460424.98084	-16984.77	1.23	
2460424.98694	-16988.93	1.21	
2460424.99312	-16987.96	1.25	
2460424.99916	-16990.45	1.17	
2460425.00528	-16992.65	1.23	
2460425.01144	-16994.04	1.23	
2460425.01742	-16995.77	1.26	
2460425.02376	-16997.55	1.30	
2460425.02975	-17004.45	1.27	
2460425.03595	-17007.00	1.30	
2460425.04212	-17010.01	1.27	
2460425.04819	-17013.93	1.25	
2460425.05416	-17016.76	1.23	
2460425.06034	-17018.99	1.25	
2460425.06654	-17021.45	1.25	
2460425.07282	-17024.00	1.24	
2460425.07882	-17025.82	1.18	
2460425.08472	-17029.31	1.23	
2460425.09108	-17032.31	1.34	
2460425.09708	-17034.72	1.28	

the BATMAN Python package (Kreidberg 2015) and the radial velocity data were modeled using the equations in Hirano et al. (2011), which solve for the anomalous radial velocity arising from the R–M effect. Following the adopted orbital parameters in Johns et al. (2019), we assumed a circular orbit. For the joint fit, we utilized a joint likelihood function of the form

$$ln L_{\text{tot}} = ln L_{\text{T}} + ln L_{\text{K}}$$
(1)

where the likelihood of a model given the data is Gaussian in nature. For the TESS data, the likelihood takes the form

$$\ln L_{\rm T} = -\frac{1}{2} \sum_{i} \left[\frac{(y_{{\rm T},i} - f(t_{{\rm T},i}; \, \theta_{\rm T}))^2}{\sigma_{{\rm T},i}^2} - \log \sigma_{{\rm T},i}^2 \right].$$
 (2)

Here, $t_{\mathrm{T},i}$, $y_{\mathrm{T},i}$, and $\sigma_{\mathrm{T},i}$ are the time, flux, and flux error of the ith data point, respectively. To account for additional astrophysical and instrumental noise in the TESS data, we define $\sigma_{\mathrm{T},i}^2 = \sigma_{m,\mathrm{T},i}^2 + \sigma_{s,\mathrm{T}}^2$, where $\sigma_{m,\mathrm{T},i}$ is the measurement uncertainty of the data point and $\sigma_{s,\mathrm{T}}$ is a systematic error term for which we fit. For the KPF data, the likelihood takes the

form

$$\ln L_{K} = -\frac{1}{2} \sum_{i} \left[\frac{(y_{K,i} - f(t_{K,i}; \theta_{K}))^{2}}{\sigma_{K}^{2}} - \log \sigma_{K}^{2} \right].$$
 (3)

Again, $t_{K,i}$ and $y_{K,i}$ are the time and radial velocity of the ith data point. For the radial velocity model, we do not include the individual radial velocity measurement uncertainties and instead treat σ_K as a free parameter. This is because the current KPF pipeline tends to overestimate measurement uncertainties, making it impossible to constrain radial velocity jitter (the equivalent of $\sigma_{s,K}$) in our case.

The model parameters (θ) for the transit and radial velocity models are defined in Table 2 and include five shared free parameters, four free parameters that belong to only the transit model, and eight free parameters that belong only to the radial velocity model. Each of the free parameters is assigned a uniform prior. The models for the two data sets are denoted by $f(t_i, \theta)$. For the transit model, this function is

$$f_{\rm T}(t_{\rm T,}i;\theta_{\rm T}) = {\rm BM}(t_{\rm T,}i;T_0;P_{\rm orb};R_{\rm p}/R_{\star};a/R_{\star};i;q_1;q_2) + \gamma_{\rm T}$$
(4)

where BM is the output of BATMAN and $\gamma_{\rm T}$ is a flux offset term. For the radial velocity model, this function is

$$f_{K}(t_{K,i}; \theta_{K}) = RM(t_{K,i}; T_{0}; P_{\text{orb}}; R_{p}/R_{\star}; a/R_{\star}; i; \lambda; \times v \sin i_{\star}; i_{\star}; u_{1}; u_{2}) + \gamma_{K} + \dot{\gamma}_{K}(t_{i} - t_{0})$$
 (5)

where RM is the output of the R-M model defined in Hirano et al. (2011), $\gamma_{\rm K}$ is a radial velocity offset term, $\dot{\gamma}_{\rm K}$ is a radial velocity slope term, and t_0 is the time of the first KPF observation. The radial velocity offset and slope terms are intended to estimate the reflex motion of the star due to the planet and any other companions in the system as well as stellar activity, which are approximately linear over the timescale of our observation for inactive stars. In the R-M model, we assumed a microturbulent velocity of 0.7 km s⁻¹, a macroturbulent velocity of 4.18 km s⁻¹ (solved for using Equation (1) of Valenti & Fischer (2005) with $T_{\rm eff} = 5899$ K), a natural line width of 1 km s⁻¹, and an instrumental Gaussian dispersion of 1.56 km s⁻¹ (the KPF linespread function width). Lastly, we note that we ignored the effects of differential rotation and convective blueshift. The effects of differential rotation are negligible at small $v \sin i_{\star}$. Convective blueshift is known to cause radial velocity signals of magnitudes of ~ 2 m s⁻¹, but often generally does not impact the measured value of λ significantly (e.g., Rubenzahl et al. 2021; Handley et al. 2025).19

 $[\]overline{^{19}}$ When including convective blueshift in the model, we recovered an obliquity of $\lambda=181.8^{+5.8\circ}_{-5.6}$, which agrees well with that recovered by the convective-blueshift-free model, and a largely unconstrained convective blueshift velocity of $v_{cb}=-233^{+166}_{-148}~{\rm m~s}^{-1}.$

 Table 2

 Definitions, Priors, and Best-fit Values of the Free Parameters Utilized in the Joint DYNESTY Fit

Parameter	Description	Units	Prior	Best-fit Value
		Shared Model Paramet	ers	
$\overline{T_0}$	Transit epoch	TBJD	U(2389.815, 2389.817)	$2389.816371 \ \pm \ 0.000016$
$P_{ m orb}$	Orbital period	days	U(2.25, 2.26)	$2.255287666 \pm 0.000000051$
$R_{\rm p}/R_{\star}$	Planet-star radius ratio	•••	U(0.1, 0.2)	0.13300 ± 0.00026
a/R_{\star}	Semimajor axis over stellar radius	•••	U(5, 10)	7.615 ± 0.021
$\cos i$	Cosine of the orbital inclination		U(0.00, 0.25)	0.06884 ± 0.00088
		Transit Model Paramet	ters	
$\overline{q_1}$	TESS quadratic limb darkening coeff. 1		<i>U</i> (0, 1)	0.350 ± 0.029
q_2	TESS quadratic limb darkening coeff. 2	•••	$\mathcal{U}(0, 1)$	0.138 ± 0.051
γ_{T}	TESS flux baseline		$\mathcal{U}(-1, 1)$	0.000201 ± 0.000014
$\ln\sigma_{s,T}$	Natural logarithm of TESS scatter		U(-20, 0)	$-8.350^{+0.085}_{-0.100}$
		R-M Model Paramete	ers	
λ	Sky-projected stellar obliquity	degrees	<i>U</i> (0, 360)	$180.4^{+4.9}_{-4.7}$
$v \sin i_{\star}$	Sky-projected stellar rotational velocity	$\mathrm{km}\ \mathrm{s}^{-1}$	U(0, 5)	$0.468^{+0.044}_{-0.043}$
$\cos i_{\star}$	Cosine of the stellar inclination	•••	$\mathcal{U}(0, 1)$	0.51 ± 0.34
u_1	KPF quadratic limb darkening coeff. 1	•••	$\mathcal{U}(0, 1)$	$0.63^{+0.23}_{-0.28}$
u_2	KPF quadratic limb darkening coeff. 2	•••	$\mathcal{U}(0, 1)$	$0.57^{+0.29}_{-0.33}$
$\gamma_{\rm K}$	KPF radial velocity baseline	$\mathrm{m}~\mathrm{s}^{-1}$	$\mathcal{U}(-16980, -16920)$	-16952.29 ± 0.45
$\dot{\gamma}_{\mathrm{K}}$	KPF radial velocity slope	$\mathrm{m}\ \mathrm{s}^{-1}\ \mathrm{day}^{-1}$	U(-500, -400)	$-434.65^{+3.65}_{-3.69}$
$\ln \sigma_{\rm K}$	Natural logarithm of KPF uncertainty	$\ln {\rm m} {\rm s}^{-1}$	U(-20, 10)	$-0.07^{+0.15}_{-0.13}$
		Derived Quantities		
i	Orbital inclination	degrees		$86.052^{+0.051}_{-0.050}$
b	Transit impact parameter			0.5243 ± 0.0053

Note. Best-fit values and their uncertainties are the 16th, 50th, and 84th percentiles of the posterior distributions. For the priors, U(l,u) represents a uniform distribution with lower and upper bounds of l and u, respectively. TBJD is the TESS BJD, defined as TBJD = BJD - 2457000.

The DYNESTY sampler was initialized with the default settings, which included 500 live points, multiple bounding ellipsoids for prior bound approximation, and a random walk sampling of the likelihood space. The sampler was terminated when the condition $\log(z+z_r) - \log z < 0.01$ was satisfied, where z is the current evidence from all saved samples and z_r is the estimated contribution to the evidence from the remaining likelihood volume. The results of this fit are shown in Table 2 and Figure 1.

We measured a sky-projected stellar obliquity of $\lambda = 180.4^{+4.9}_{-4.7}$, indicating an orbit that is retrograde relative to the stellar spin. We also precisely measured the sky-projected stellar rotational velocity from the R-M fit to be $v \sin i_{\star} = 0.468^{+0.044}_{-0.043} \ \mathrm{km \ s^{-1}}$, which is relatively low for a Solar-type star (note that a uniform prior of 0-5 km s⁻¹ was assumed for $v \sin i_{\star}$ in the fit). This may suggest a nearly face-on stellar spin axis. Based on the analysis in Johns et al. (2019), the system has an age of $6.4^{+3.5}_{-3.2}$ Gyr, for which Sun-like stars

typically exhibit rotation periods of 20–40 days (Barnes 2007; Mamajek & Hillenbrand 2008; Angus et al. 2015). For KELT-23A, these rotation periods correspond to stellar inclinations between roughly 10° and 20° assuming a stellar radius of $R_{\star}=0.996\pm0.015\,R_{\odot}$ (Johns et al. 2019). This range of stellar inclination angles would translate to true 3-dimensional stellar obliquities between roughly 95° and 110° , or a near-polar orbit (Masuda & Winn 2020). We note that a similar argument for a polar orbit was made by Winn et al. (2009) for HAT-P-7, another multi-star system with a HJ for which $\lambda \sim 180^{\circ}$.

We emphasize that this is a purely speculative exercise. It is possible that the spin of KELT-23A has been slowed due to tidal interactions with its close-in HJ (see Section 4 for a more detailed discussion). Ultimately, a measurement of the stellar rotation period is required to calculate the actual stellar inclination and 3D stellar obliquity. While it is possible to measure the rotation period of a star based on starspot-driven modulation of its light curve, we found no strong evidence of strong modulation in the TESS data.

 $[\]overline{^{20}}$ We note that the corner plot between λ and $v \sin i_{\star}$ revealed no noticeable covariance between the two variables.

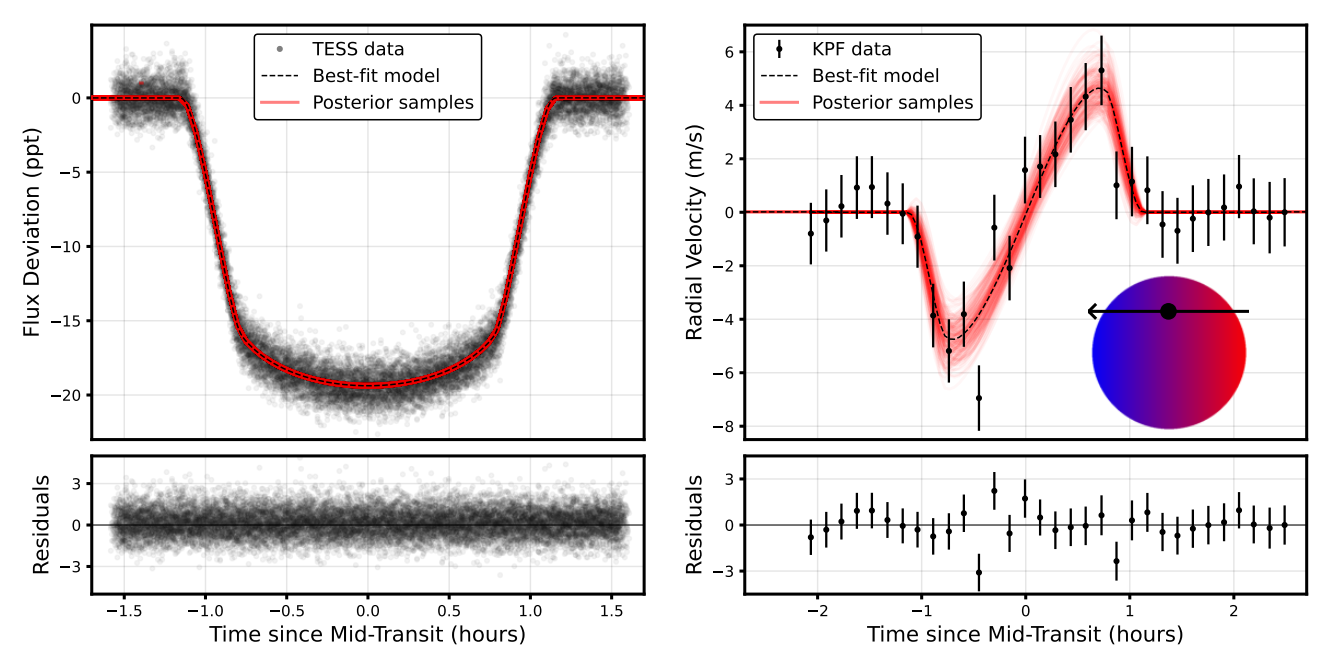


Figure 1. Results of the joint DYNESTY fit to the TESS photometry (left) and KPF radial velocities (right). A diagram of the best-fit transit is shown in the right-hand panel, where the color of the stellar surface indicates whether it is blueshifted and redshifted. The black points are the data, the dashed black lines are the best-fit (median) models, and the solid red lines are random samples from the posterior distributions (200 in total). The TESS data is phase folded to the best-fit period and transit epoch. The offset and slope have been removed from the radial velocity data for visual clarity.

3.2. The Orbit of KELT-23B

Following Behmard et al. (2022), we used Gaia DR3 to precisely measure the relative positions and velocity vectors of the two stars KELT-23A and KELT-23B (also see Tokovinin & Kiyaeva 2016). The angle between the relative position vector and relative velocity vector, typically denoted γ , contains information about the orbit of the pair of stars around their center of mass. For instance, $\gamma=0^\circ$ suggests that we are viewing the system edge-on whereas $\gamma=90^\circ$ suggests that we are viewing the system face-on (assuming a near-circular orbit). When combined with the measured obliquity of the primary star, this angle can reveal information about the origin and evolution of the system (e.g., Behmard et al. 2022; Rice et al. 2024).

For the KELT-23 system, we measured $\gamma = 60^{\circ} \pm 4^{\circ}$, suggesting that the pair of stars orbit one another closer to a face-on orientation than an edge-on orientation. We further discuss the implications of this angle in Section 4.

4. Discussion

We place KELT-23A into context with other stars with HJ companions (defined here as planets with $M_{\rm p}=0.3-13\,M_{\rm Jup}$ and $a/R_{\star}<10$) in Figure 2. This figure, which plots sky-projected stellar obliquity against stellar effective temperature, showcases the sharp transition between the mostly low obliquities of cool stars with HJs and the high obliquities of hot stars with HJs. First noted by Winn et al. (2010) to occur near the Kraft break

(Kraft 1967), this transition is likely a consequence of different tidal realignment efficiencies in stars with different internal energy transport structures (Albrecht et al. 2022). KELT-23A stands out as one of the only cool stars known to have a high stellar obliquity relative to its HJ companion, the other three being WASP-60 ($|\lambda|=129^{\circ}\pm17^{\circ}$; Mancini et al. 2018), WASP-94A ($|\lambda|=123^{\circ}\pm3^{\circ}$; Neveu-VanMalle et al. 2014; Ahrer et al. 2024), and TOI-858B ($|\lambda|=99.3^{+3.8}_{-3.7}$; Hagelberg et al. 2023). We note that this figure excludes stars with λ uncertainties greater than 30°. It also excludes the stars CoRoT-1, CoRoT-19, HATS-14, WASP-1, WASP-2, and WASP-23 due to their λ measurements being unreliable (see Albrecht et al. 2022 for more details).

Interestingly, three of the four cool stars with HJs on misaligned orbits—KELT-23A, WASP-94A, and TOI-858B—have wide-separation stellar companions. KELT-23A has an M dwarf companion with a projected separation of 570 au, WASP-94A has a late F-type companion with a projected separation of 2700 au, and TOI-858B has a late F-type companion with a projected separation of 3000 au. This trend hints that outer companions play a role in misaligning HJs around cool stars. One possible scenario involves the HJ beginning its life on an initially distant orbit that had its eccentricity and inclination excited via von Zeipel–Lidov–Kozai (ZLK) interactions with the wide-separation stellar companions (von Zeipel 1910; Kozai 1962; Lidov 1962), after which tidal interactions with the host star induced rapid orbital shrinking and circularization (Fabrycky & Tremaine 2007).

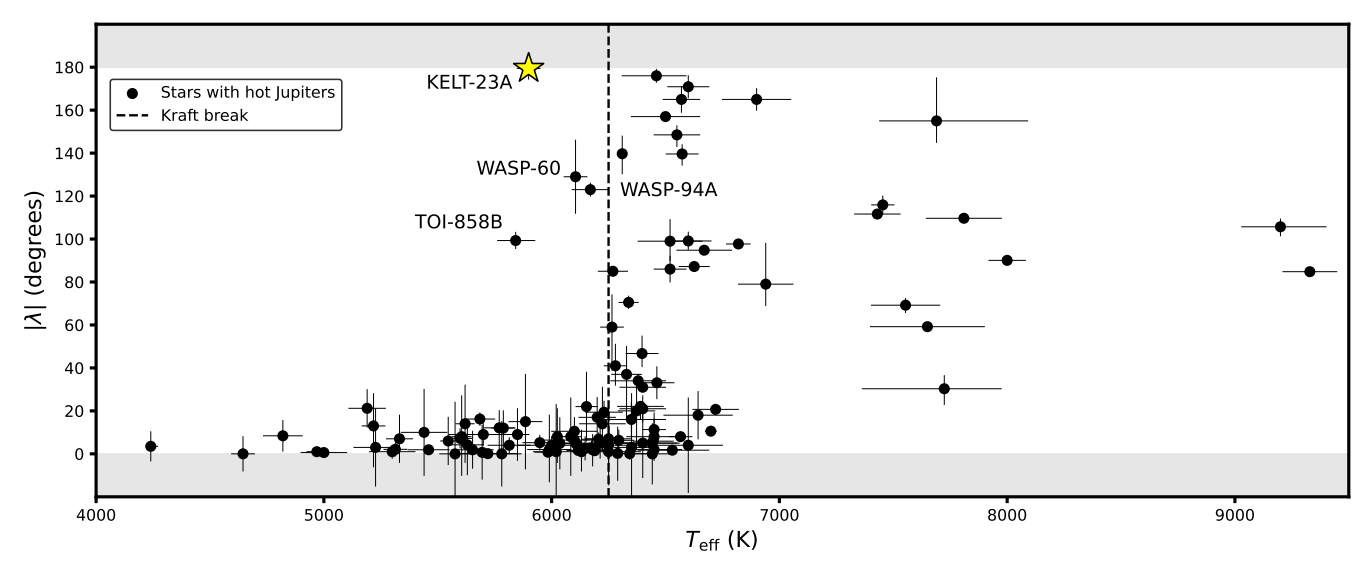


Figure 2. Sky-projected stellar obliquity (λ) vs. stellar effective temperature ($T_{\rm eff}$) for stars with HJs (planets with $M_{\rm p}=0.3$ –13 $M_{\rm Jup}$ and $a/R_{\star}<10$). The yellow star is KELT-23A and the dashed line is the Kraft break ($T_{\rm Kraft}\approx6250$ K). Systems with λ uncertainties greater than 30° or with unreliable λ measurements are excluded (see Section 4). KELT-23A is one of few cool stars with a HJ on a retrograde orbit ($|\lambda|>90^{\circ}$). The three other cool stars with HJs on misaligned orbits are labeled: WASP-60 (Mancini et al. 2018), WASP-94A (Neveu-VanMalle et al. 2014; Ahrer et al. 2024), and TOI-858B (Hagelberg et al. 2023). Like KELT-23A, the latter two of these systems have binary star companions, potentially suggesting a link between stellar multiplicity and spin–orbit misalignment. Data acquired from TEPCat on 2025 May 1 (Southworth 2011).

Observational and theoretical studies have suggested that this mechanism may be responsible for an appreciable fraction (although likely no more than ~50%) of HJs (Naoz et al. 2012; Dawson et al. 2015; Petrovich 2015a; Anderson et al. 2016; Muñoz et al. 2016; Ngo et al. 2016). Star-planet ZLK interactions are also among the most favored mechanisms for producing planets on polar and retrograde orbits, making it a particularly compelling explanation for this subsample of the HJ population. In principle, it is also possible that the presence of binary companions triggered primordial spin—orbit misalignments due to nascent star-disk interactions (Batygin 2012; Batygin & Adams 2013; Lai 2014; Spalding & Batygin 2014; Matsakos & Königl 2017; Zanazzi & Lai 2018a, 2018b).

Alternatively, these planets could have been driven inwards due to interactions with unknown planetary-mass companions with wide orbital separations (e.g., Chatterjee et al. 2008; Wu & Lithwick 2011; Beaugé & Nesvorný 2012; Petrovich 2015b; Petrovich & Tremaine 2016; Teyssandier et al. 2019). Radial velocity surveys of single-star systems have found that nearly all stars with close-in Jupiter-mass companions have another planetary companion of equal or greater mass on a more distant orbit (Zink & Howard 2023). Some of these planet-planet interaction mechanisms are believed to be capable of producing HJs on retrograde orbits (Beaugé & Nesvorný 2012; Lithwick & Wu 2014; Petrovich & Tremaine 2016). It is plausible that the presence of a wide stellar binary companion facilitates interactions between the two planets that ultimately drives one inwards (e.g., Yang et al. 2025).

Regardless of how KELT-23A b and similar planets arrived at their close-in orbits, we must also address the issue of how the planet has retained a retrograde orbit over a long timescale. While the exact tidal mechanisms responsible for spin-orbit realignment are still up for debate (Albrecht et al. 2022), most predict that cool stars should achieve realignment on relatively short timescales (e.g., Winn et al. 2010; Dawson 2014; Zanazzi et al. 2024; Zanazzi & Chiang 2025). One possible explanation is that the planetary orbit has "stalled" at an antialigned or polar orientation. Using equilibrium tide and inertial wave dissipation models, Xue et al. (2014) and Li & Winn (2016) showed that this stalling can last many billions of years and usually coincides with a slowing of the stellar rotation rate, possibly explaining the low $v \sin i_{\star}$ of KELT-23A (also see Lai 2012). Lastly, we cannot rule out the possibility that KELT-23A b arrived at its close-in orbit relatively recently and is currently in the process of having its orbit realigned with the stellar spin. Depending on the rate of spin-orbit realignment, it may be inevitable that some HJs orbiting cool stars will be caught in the act.

4.1. Toy Model and Population Synthesis

To better understand the role stellar companions have on the production of HJs, we plotted λ and γ for cool stars ($T_{\rm eff} < 6250$ K) and hot stars ($T_{\rm eff} > 6250$ K) with stellar binary companions and HJ companions in Figure 3. Numerical simulations have suggested that these wide binary companions may play prominent roles in disrupting planetary systems, potentially producing HJs in the process (e.g., Kaib et al. 2013).

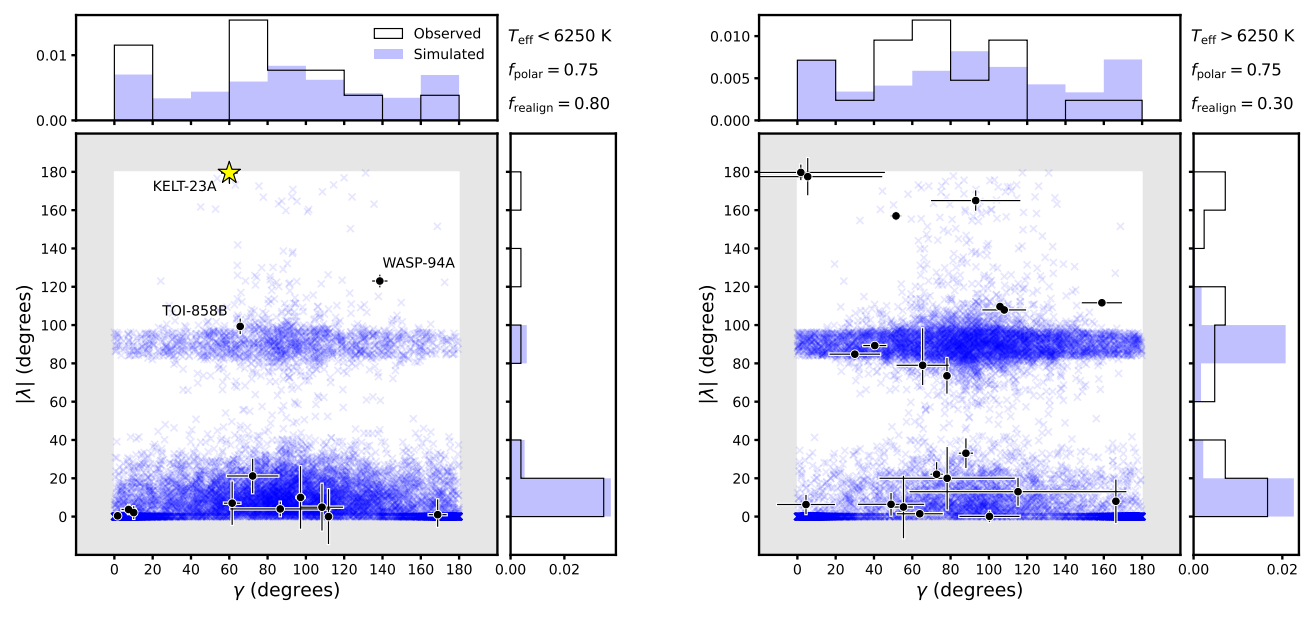


Figure 3. Sky-projected stellar obliquity (λ) vs. sky-projected binary orbit angle (γ) for cool stars (left; $T_{\rm eff} < 6250$ K) and hot stars (right; $T_{\rm eff} > 6250$ K) with stellar binary companions and HJ companions ($M_{\rm p} = 0.3-13~M_{\rm Jup}$ and $a/R_{\star} < 10$). Black circles are the observed data and blue X's are simulated data from the toy model in Section 4.1. Normalized histograms of the data are shown in the margins. Observed systems with λ uncertainties greater than 30° or with unreliable λ measurements are excluded (see Section 4). Values of γ for KELT-23A ($\gamma = 60^{\circ} \pm 4^{\circ}$) and TOI-858B ($\gamma = 65^{\circ}, 7 \pm 0.5^{\circ}$) were calculated using the approach in Behmard et al. (2022). For the remaining systems, we adopted the values of γ from Rice et al. (2024). Our toy model can reproduce the most salient features of the distribution, namely the excess of systems near $\gamma = 90^{\circ}, \gamma = 0^{\circ}$, and $\gamma = 180^{\circ}$, and the dearth of systems with $|\lambda|$ between 40° and 80°.

Based on the (albeit small-numbered) distribution in Figure 3, there appears to be a preference for HJs in binary star systems to be found when the binary orbit is near face-on ($\gamma=90^\circ$) or near edge-on ($\gamma=0^\circ$ or $\gamma=180^\circ$). We note that this pattern was first identified by Behmard et al. (2022) and was later disputed by Rice et al. (2024) using a larger sample of systems that included non-HJ planets.

To determine whether this distribution can be reproduced via interactions between the planet (or the disk in which it formed) and the binary companion, we constructed a toy model and performed a population synthesis simulation of the resulting values of λ and γ . The model, which is visualized in Figure 4, is set up as follows:

1. Establish a system with a Jovian planet on a 1-10 au orbit and a $0.5\,M_\odot$ stellar companion on a 1000 au orbit around a Solar-type star. Assume that the orbit of the planet and the stellar companion are approximately coplanar and aligned with the equator of the primary star, a configuration that recent papers have suggested may be common for systems with small, close-in planets (Christian et al. 2025; Rice et al. 2024). Given that Jovian planets likely form in similar disks and that the orbits of warm Jupiters tend to be aligned with the equators of their host stars (Rice et al. 2022b), it is reasonable to extrapolate this trend to the cold Jupiters considered here.

- 2. Sample initial orbital parameters for the system. Assume the possible orbital eccentricities of the stellar companion are uniformly distributed between 0 and 1, 21 the cosine of the possible orbital inclinations are uniformly distributed between 0 and 1, and the possible arguments of periastron, arguments of ascending node, and true anomaly are uniformly distributed between 0 and 2π . Transform the resulting orbital positions and motions into celestial coordinates and calculate γ .
- 3. Assume the Jovian planet is driven inward via some unspecified mechanism and becomes a HJ with a 3 days orbital period, which corresponds to $a/R_{\star}=8.75$ for a Solar-type star. Assume that the planet obtains a polar orbit with a frequency of $f_{\rm polar}$ and an aligned orbit with a frequency of $1-f_{\rm polar}$ (e.g., Albrecht et al. 2021). If the planet obtains a polar orbit, randomly draw an angle ϕ from a uniform distribution between 0 and π , where ϕ is the rotation angle of the orbit normal about the stellar rotation axis (i.e., if the stellar spin axis points along the y axis, ϕ describes where the orbit normal, which is always orthogonal to the y axis for a polar orbit, points in the x-z plane).

 $[\]overline{^{21}}$ In principle, very high eccentricities ($e \gtrsim 0.9$) can be excluded because the binary companions would disrupt the protoplanetary disks. In any case, we found that the results of the simulation are not strongly sensitive to variations of $e_{\rm max}$ between 0.8 and 1.0.

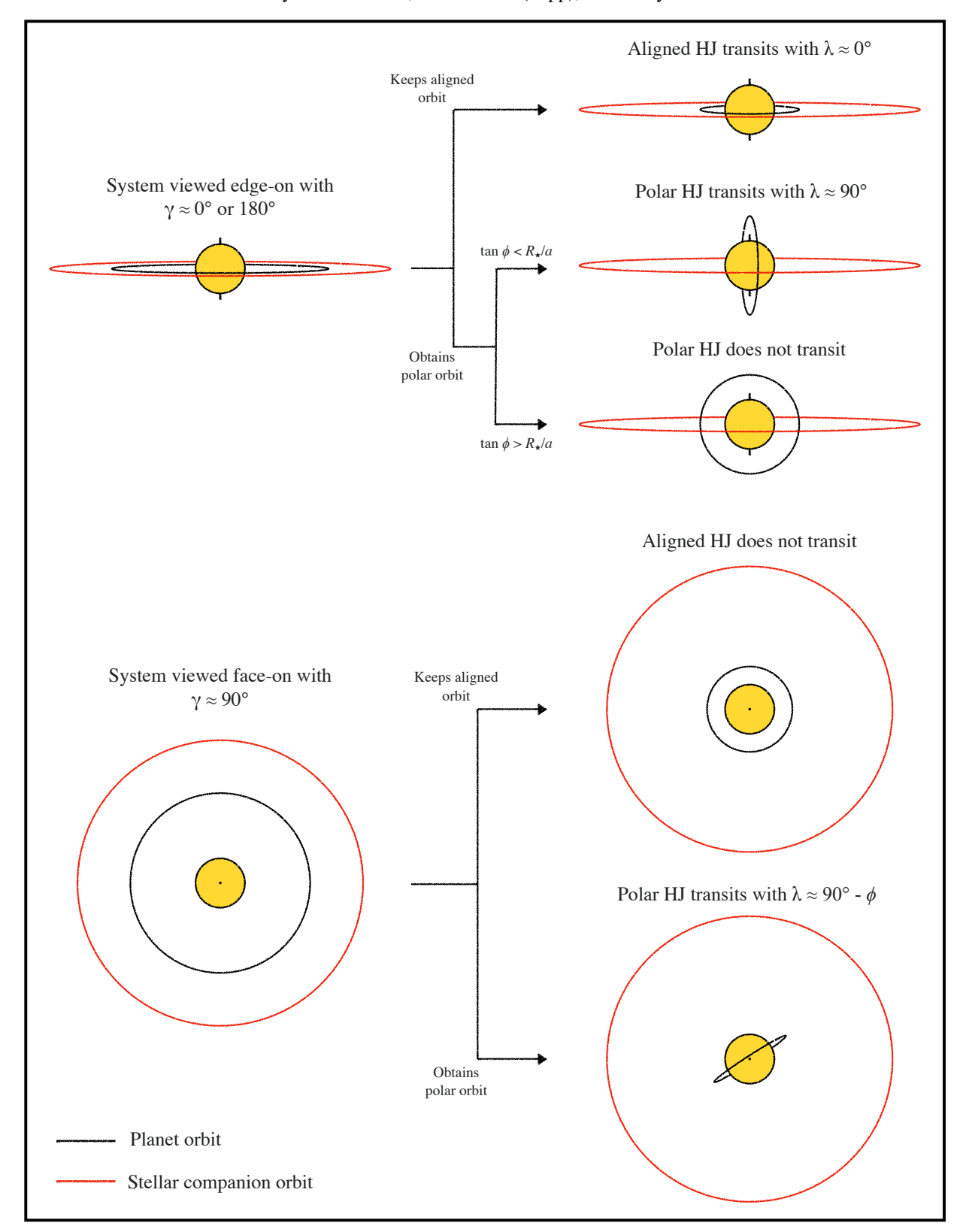


Figure 4. Visualizations of the two extreme cases of the toy model in Section 4.1, in which the initial system is viewed edge-on (top) and face-on (bottom), and their possible outcomes. Initially edge-on systems generally produce transiting HJs with $\lambda \approx 0^{\circ}$ or $\lambda \approx 90^{\circ}$. Initially face-on systems only produce HJs that transit when the HJ is in a polar orbit. A wide range of λ values are possible for these systems, where $\lambda \approx 90^{\circ} - \phi$ (note that i_{\star} must be non-zero, else the R–M signal would be undetectable).

- 4. If the HJ obtains a polar orbit, assume there is a probability of $f_{\rm realign}$ that the star realigns with the planet orbit before we observe it. If the star does realign, draw the final value of λ from a half-Normal distribution with a mean of 0° and a standard deviation of 15° .
- 5. Determine if the resulting HJ transits and, if it does, calculate λ . In terms of the initial orbital inclination of the planet (i_0) and ϕ , the condition for a polar HJ to transit is $\sin i_0 \tan \phi < R_{\star}/a$. For simplicity, we assume $\lambda \approx 90^{\circ} \phi$, which is accurate to within a few degrees.
- 6. Repeat steps 1-5 N times to generate a population.

The result of this simulation for $N = 10^5$ is shown in Figure 3. Based on visual inspection, we found that $f_{\text{polar}} = 0.75$ with $f_{\rm realign} = 0.80$ most closely reproduces the observed distribution for cool stars and $f_{\text{polar}} = 0.75$ with $f_{\text{realign}} = 0.30$ most closely reproduces the observed distribution for hot stars. The toy model broadly reproduces the most salient features of the observed distributions, namely the preference for transiting HJs to be in systems with γ near 0° , 90° , and 180° , in addition to the preference for values of λ near 0° and 90° (Albrecht et al. 2021). The model is able to produce systems with $|\lambda|$ between 90° and 180°, accounting for systems like KELT-23A and WASP-94A, but underpredicts the number of these systems we should observe. In addition, there may be an observational bias against systems with high λ , because these systems are more likely to have stars spinning face-on with lower values of $v \sin i_{\star}$ (and therefore lower R-M amplitudes), meaning the fraction of systems in these highly misaligned orientations may be even higher than the current data suggests. This implies that a non-negligible fraction of HJs arrive near their host stars with true retrograde, non-polar orbits and remain in those orientations for long enough to be observed.

It is interesting to compare our chosen value of $f_{\rm polar}$ to those predicted by different migration mechanisms. As mentioned previously, most mechanisms struggle to produce systems with polar or retrograde orbits, with planet–planet ZLK and planet-star ZLK being the most efficient (Anderson et al. 2016; Petrovich & Tremaine 2016). However, these mechanisms are only predicted to produce planets on polar or retrograde orbits 25%–50% of the time, making them inconsistent with the results of our toy model. Primordial misalignment mechanisms involving interactions between the protoplanetary disk and the stellar companion may offer a more compelling explanation (Batygin 2012; Batygin & Adams 2013; Lai 2014; Spalding & Batygin 2014; Matsakos & Königl 2017; Zanazzi & Lai 2018a, 2018b).

5. Conclusion

Using the KPF spectrograph, we measured the sky-projected stellar obliquity of the Sun-like star KELT-23A, which hosts a transiting HJ companion with an orbital period of 2.26 days (Johns et al. 2019). By jointly fitting the TESS and KPF data of the star, we found $\lambda = 180.4^{+4.9\circ}_{-4.7}$ and $(\nu \sin i_{\star} = 0.468^{+0.043}_{-0.043} \text{ km s}^{-1})$,

indicating a retrograde orbit and a slow sky-projected stellar rotational velocity. This low value of $v \sin i_{\star}$ may suggest that the stellar spin axis is being viewed close to face-on, which would mean the true obliquity is close to polar. This is one of a few stars with an effective temperature below the Kraft break that has a HJ on a misaligned orbit, providing an interesting case study of HJs orbiting cool stars that have not yet had their orbits realigned with the stellar spin by tides. In particular, the observed obliquity of KELT-23A may be consistent with realignment theories involving equilibrium tides and inertial wave dissipation, which predict that the orbits of HJs can stall at antialigned and polar orientations for Gyr timescales (Xue et al. 2014; Li & Winn 2016).

We explored the role that the wide-separation stellar companion KELT-23B may have played in creating a HJ with a retrograde orbit. When examining the sky-projected binary orbit angles (γ) of binary systems in which one star hosts a HJ with a λ measurement, systems tend to clump near face-on binary orbits ($\gamma=90^{\circ}$) and edge-on binary orbits ($\gamma=0^{\circ}$ and $\gamma=180^{\circ}$) (Behmard et al. 2022). We found that this distribution can be broadly reproduced using a toy model in which a HJ begins its life on a distant orbit that is coplanar with both the equator of the primary star and the orbit of the wide-separation stellar companion, after which it migrates inwards and preferentially obtains an orbit that is either aligned with the stellar equator or polar.

Acknowledgments

We thank Heather A. Knutson, Joshua N. Winn, Jessie L. Christiansen, and Kevin Hardegree-Ullman for their helpful discussions involving this paper.

The data presented herein were obtained at the W. M. Keck Observatory, which is operated as a scientific partnership among the California Institute of Technology, the University of California, and the National Aeronautics and Space Administration. The Observatory was made possible by the generous financial support of the W. M. Keck Foundation. Keck Observatory occupies the summit of Maunakea, a place of significant ecological, cultural, and spiritual importance within the indigenous Hawaiian community. We understand and embrace our accountability to Maunakea and the indigenous Hawaiian community, and commit to our role in long-term mutual stewardship. We are most fortunate to have the opportunity to conduct observations from Maunakea.

We gratefully acknowledge the efforts and dedication of the Keck Observatory staff for support of KPF and remote observing. S.G. is supported by an NSF Astronomy and Astrophysics Postdoctoral Fellowship under award AST-2303922. A.W.H. acknowledges funding support from NASA grant No. 80NSSC24K0161.

The research was carried out, in part, at the Jet Propulsion Laboratory, California Institute of Technology, under a contract with the National Aeronautics and Space Administration (80NM0018D0004)

Facilities: TESS, Keck:I (KPF).

Software: BATMAN (Kreidberg 2015), DYNESTY (Speagle 2020).

ORCID iDs

```
Steven Giacalone https://orcid.org/0000-0002-8965-3969
Andrew W. Howard https://orcid.org/0000-0001-8638-0320
Ryan A. Rubenzahl https://orcid.org/0000-0003-3856-3143
Fei Dai https://orcid.org/0000-0002-8958-0683
Luke B. Handley https://orcid.org/0000-0002-9305-5101
Howard Isaacson https://orcid.org/0000-0002-0531-1073
Samuel Halverson https://orcid.org/0000-0003-1312-9391
Max Brodheim https://orcid.org/0009-0008-9808-0411
William Deich https://orcid.org/0009-0000-3624-1330
Benjamin J. Fulton https://orcid.org/0000-0003-3504-5316
Steven R. Gibson https://orcid.org/0009-0004-4454-6053
Grant M. Hill https://orcid.org/0000-0002-7648-9119
Bradford Holden https://orcid.org/0000-0002-6153-3076
Aaron Householder https://orcid.org/0000-0002-5812-3236
Russ R. Laher https://orcid.org/0000-0003-2451-5482
Kyle Lanclos https://orcid.org/0009-0004-0592-1850
Joel Payne https://orcid.org/0009-0008-4293-0341
Erik A. Petigura https://orcid.org/0000-0003-0967-2893
Arpita Roy https://orcid.org/0000-0001-8127-5775
Christian Schwab https://orcid.org/0000-0002-4046-987X
Martin M. Sirk https://orcid.org/0009-0007-8555-8060
Josh Walawender https://orcid.org/0000-0002-6092-8295
```

References

```
Ahrer, E., Seidel, J. V., Doyle, L., et al. 2024, MNRAS, 530, 2749
Albrecht, S., Winn, J. N., Johnson, J. A., et al. 2012, ApJ, 757, 18
Albrecht, S. H., Dawson, R. I., & Winn, J. N. 2022, PASP, 134, 082001
Albrecht, S. H., Marcussen, M. L., Winn, J. N., Dawson, R. I., &
   Knudstrup, E. 2021, ApJL, 916, L1
Anderson, K. R., Storch, N. I., & Lai, D. 2016, MNRAS, 456, 3671
Angus, R., Aigrain, S., Foreman-Mackey, D., & McQuillan, A. 2015,
    MNRAS, 450, 1787
Barnes, S. A. 2007, ApJ, 669, 1167
Batygin, K. 2012, Natur, 491, 418
Batygin, K., & Adams, F. C. 2013, ApJ, 778, 169
Beaugé, C., & Nesvorný, D. 2012, ApJ, 751, 119
Behmard, A., Dai, F., & Howard, A. W. 2022, AJ, 163, 160
Chatterjee, S., Ford, E. B., Matsumura, S., & Rasio, F. A. 2008, ApJ, 686, 580
Christian, S., Vanderburg, A., Becker, J., et al. 2025, AJ, 169, 308
Dawson, R. I. 2014, ApJL, 790, L31
Dawson, R. I., & Johnson, J. A. 2018, ARA&A, 56, 175
Dawson, R. I., Murray-Clay, R. A., & Johnson, J. A. 2015, ApJ, 798, 66
Dong, J., & Foreman-Mackey, D. 2023, AJ, 166, 112
```

```
Fabrycky, D., & Tremaine, S. 2007, ApJ, 669, 1298
Gibson, S. R., Howard, A. W., Rider, K., et al. 2024, Proc. SPIE, 13096,
Hagelberg, J., Nielsen, L. D., Attia, M., et al. 2023, A&A, 679, A70
Handley, L. B., Howard, A. W., Rubenzahl, R. A., et al. 2025, AJ, 169, 212
Hirano, T., Suto, Y., Winn, J. N., et al. 2011, ApJ, 742, 69
Jenkins, J. M., Twicken, J. D., McCauliff, S., et al. 2016, Proc. SPIE, 9913,
Johns, D., Reed, P. A., Rodriguez, J. E., et al. 2019, AJ, 158, 78
Kaib, N. A., Raymond, S. N., & Duncan, M. 2013, Natur, 493, 381
Kozai, Y. 1962, AJ, 67, 591
Kraft, R. P. 1967, ApJ, 150, 551
Kreidberg, L. 2015, PASP, 127, 1161
Lai, D. 2012, MNRAS, 423, 486
Lai, D. 2014, MNRAS, 440, 3532
Li, G., & Winn, J. N. 2016, ApJ, 818, 5
Lidov, M. L. 1962, P&SS, 9, 719
Lithwick, Y., & Wu, Y. 2014, PNAS, 111, 12610
Lubin, J., Petigura, E. A., Mišić, V. V., Van Zandt, J., & Handley, L. B. 2025,
   AstroQ: Automated Scheduling of Cadenced Astronomical Observations,
   arXiv:2506 08195
Mamajek, E. E., & Hillenbrand, L. A. 2008, ApJ, 687, 1264
Mancini, L., Esposito, M., Covino, E., et al. 2018, A&A, 613, A41
Masuda, K., & Winn, J. N. 2020, AJ, 159, 81
Matsakos, T., & Königl, A. 2017, AJ, 153, 60
McLaughlin, D. B. 1924, ApJ, 60, 22
Moe, M., & Di Stefano, R. 2017, ApJS, 230, 15
Muñoz, D. J., Lai, D., & Liu, B. 2016, MNRAS, 460, 1086
Naoz, S., Farr, W. M., & Rasio, F. A. 2012, ApJL, 754, L36
Neveu-VanMalle, M., Queloz, D., Anderson, D. R., et al. 2014, A&A,
   572, A49
Ngo, H., Knutson, H. A., Hinkley, S., et al. 2016, ApJ, 827, 8
Petrovich, C. 2015a, ApJ, 799, 27
Petrovich, C. 2015b, ApJ, 805, 75
Petrovich, C., & Tremaine, S. 2016, ApJ, 829, 132
Rice, M., Gerbig, K., & Vanderburg, A. 2024, AJ, 167, 126
Rice, M., Wang, S., & Laughlin, G. 2022a, ApJL, 926, L17
Rice, M., Wang, S., Wang, X.-Y., et al. 2022b, AJ, 164, 104
Ricker, G. R., Winn, J. N., Vanderspek, R. K., et al. 2015, JATIS, 1, 014003
Rossiter, R. A. 1924, ApJ, 60, 15
Rubenzahl, R. A., Dai, F., Howard, A. W., et al. 2021, AJ, 161, 119
Schwab, C., Stürmer, J., Gurevich, Y. V., et al. 2015, PASP, 127, 880
Siegel, J. C., Winn, J. N., & Albrecht, S. H. 2023, ApJL, 950, L2
Southworth, J. 2011, MNRAS, 417, 2166
Spalding, C., & Batygin, K. 2014, ApJ, 790, 42
Speagle, J. S. 2020, MNRAS, 493, 3132
Teyssandier, J., Lai, D., & Vick, M. 2019, MNRAS, 486, 2265
Tokovinin, A., & Kiyaeva, O. 2016, MNRAS, 456, 2070
Valenti, J. A., & Fischer, D. A. 2005, ApJS, 159, 141
von Zeipel, H. 1910, AN, 183, 345
Winn, J. N., Fabrycky, D., Albrecht, S., & Johnson, J. A. 2010, ApJL,
   718, L145
Winn, J. N., Johnson, J. A., Albrecht, S., et al. 2009, ApJL, 703, L99
Wu, Y., & Lithwick, Y. 2011, ApJ, 735, 109
Xue, Y., Suto, Y., Taruya, A., et al. 2014, ApJ, 784, 66
Yang, E., Su, Y., & Winn, J. N. 2025, ApJ, 986, 117
Zanazzi, J. J., & Chiang, E. 2025, ApJ, 983, 157
Zanazzi, J. J., Dewberry, J., & Chiang, E. 2024, ApJL, 967, L29
Zanazzi, J. J., & Lai, D. 2018a, MNRAS, 477, 5207
Zanazzi, J. J., & Lai, D. 2018b, MNRAS, 478, 835
Zink, J. K., & Howard, A. W. 2023, ApJL, 956, L29
```